Noname manuscript No.
(will be inserted by the editor)

Accelerated Dynamic MRI using Kernel-Based Low Rank Constraint

Omar Arif, Hammad Afzal, Haider Abbas, Muhammad Faisal Amjad, Jiafu Wan and Raheel Nawaz

Received: date / Accepted: date

Abstract We present a novel reconstruction method for dynamic MR images from highly under-sampled k-space measurements. The reconstruction problem is posed as spectrally regularized matrix recovery problem, where kernel-based low rank constraint is employed to effectively utilize the non-linear correlations between the images in the dynamic sequence. Unlike other kernel-based methods, we use a single-step regularized reconstruction approach to simultaneously learn the kernel basis functions and the weights. The objective function is optimized using variable splitting and alternating direction method of multipliers. The framework can seamlessly handle additional sparsity constraints such as spatio-temporal total variation. The algorithm performance is evaluated on a numerical phantom and *in vivo* data sets and it shows significant improvement over the comparison methods.

Keywords Dynamic MRI reconstruction · kernel methods · low rank decomposition

O. Arif, H. Afzal and F. Amjad
National University of Sciences and Technology (NUST), Islamabad, Pakistan
E-mail: omar.arif@seecs.edu.pk,hammad.afzal@mcs.edu.pk, faisal@nust.edu.pk

H. Abbas
National University of Sciences and Technology (NUST), Islamabad, Pakistan and Florida Institute of Technology, USA.
E-mail: haidera@kth.se

J. Wan
South China University of Technology, Guangzhou, China
E-mail: mejwan@scut.edu.cn

R. Nawaz
Manchester Metropolitan University, UK.
E-mail: r.nawaz@mmu.ac.uk

1 Introduction

In magnetic resonance imaging (MRI), parts of the body are excited by a radio frequency pulse, which excites the spins in the 2D slice or a 3D volume of the body. The excited spins act like radio frequency emitters. For localization of the excited spins, the frequency and phase of the spins is modified using a time varying magnetic gradient fields. The magnetization state of the spins is received by the receiving coil and digitized and saved in the k-space grid. The frequency and phase-encoding are stored in the x-axis and y-axis respectively. The order in which the frequency and the phase encoding is carried out defines the trajectory of the k-space. In Cartesian trajectory, for example, the k-space is sampled row by row. During the filling of the k-space lines, motion may take place resulting in various reconstruction artifacts such as blurring. Many clinical applications require imaging an organ with high temporal resolution For example, in dynamic contrast enhanced MRI (DCE-MRI), fast imaging is required to measure the physiological tissue characteristics in the presence of a contrast agent [19, 21]. Similarly, respiratory motion during abdominal or cardiovascular imaging is also a major challenge in dynamic MRI [13]. However, MRI acquisition is a time consuming process because of various physical and physiological conditions [42]. The reconstructed images thus have a limited spatial and temporal resolution.

Researchers have looked at many approaches to accelerate the MRI acquisition time. Parallel imaging (PI) [17] is a hardware-based approach, which accelerates the acquisition time by combining the signals from several receiver coils to reconstruct the images. Compressed sensing (CS) [9, 25] is a software-based approach to accelerate MRI acquisition by incoherent k-space undersampling and using nonlinear reconstruction techniques. Cartesian trajectory achieves incoherence by under sampling the y-axis of the k-space and fully sampling the x-axis. To achieve incoherence in multiple dimensions, radial k-space trajectories [14] are used. In radial trajectory, the k-space is sampled via radial lines passing through the center of the k-space. The radial trajectories are also less sensitive to motion and therefore are standard choice for dynamic MRI [34]. By acquiring radial profile lines spaced at a constant increment of 111.25^0, which is derived from the golden ratio, uniform coverage of the k-space is insured [48]. By using the aforementioned techniques together, further reduction in the acquisition times can be achieved [12, 13, 32]. However, motion may still take place during the time it takes to sample the k-space and therefore, different k-space lines may correspond to different motion states. To avoid this, k-space profile lines are acquired at times synchronized by a gating signal so that all profile lines correspond to the same motion state [16, 38]. However, such techniques further increase the scan time and hence the patient discomfort. Self gating techniques avoid timed acquisitions, by using the k-space data itself to derive a gating signal retrospectively [7, 23]. In radial trajectories, the magnitude of the center of the k-space can be used as a 1-D self gating signal [18]. However, the performance of this approach can degrade when imaging an organ with complex motion, since the assumption of global

rigid motion is violated. To capture complex organ motion, manifold learning techniques [4] have been used to generate the self gating signal [35, 44]. [35] assumes that the images in the dynamic data set come from a low dimensional manifold. The shape of the manifold is determined by sampling the same location of the k-space for each frame. It requires sufficient large number of highly correlated frames to reliably learn the manifold. In case, when only few frames are available or the frames vary significantly in the temporal direction (e.g DCE-MRI), the performance can degrade. Similarly, Chen et. al. [8] employ locally linear embedding [37] to learn a multidimensional self gating signal directly from the k-space data, which is then used to group the k-space profiles. The reconstruction is then performed using non-linear FFT on the grouped profiles.

Since, the dynamic images are highly correlated, various techniques exploit the low rank structure of the dynamic image data to constraint the objective function [15, 20, 22, 26]. These techniques are based on Karhunen-Louve transform (KLT), which is a linear transform and hence is incapable of capturing non-linear correlations between the temporal frames. Such non-linear correlations may be quite important when imaging an organ with complex motion or in case of dynamic contrast enhanced MRI. To exploit non-linearity, [27, 28] propose a non-linear dictionary-based algorithms. Similarly, in [29, 46], a kernel-based framework is proposed to incorporate non-linear manifold models in reconstruction. The algorithm uses a two step approach. The first step estimates kernel-based temporal basis functions using zero-filled reconstruction of some central k-space data. The second step enforces the low rank constraint by projecting the data onto the most significant temporal basis functions learned in the first step. The projected data is then mapped back to the original space using preimaging with data consistency constraint. The second step is repeated until convergence. A sufficient number of central k-space data is required to obtain a good estimate of the basis functions in the first step. However increasing the central k-space encodes will result in fewer high frequency encodes. So the performance is dependent on a fine balance between the amount of low frequency and high frequency encodes [22]. In this paper, we propose a single-step regularized reconstruction framework that simultaneously learns the temporal basis functions and the spatial weights of the kernel-induced feature space. This allows for high quality reconstruction at a range of acceleration rates. The proposed method uses a Gaussian kernel to map the data to a non-linear feature space, where low rank constraint is exploited. Our method also provides a systematic way of employing additional sparsity constraints in addition to the low rank constraint. Our k-space acquisition scheme is based on golden angle radial trajectories which are less sensitive to motion [12] than the non-uniform Cartesian trajectory employed in [29].

Contributions: This paper presents a novel single step kernel-based spectrally regularized framework to effectively utilize the higher order correlations between the dynamic image series for better reconstruction. The framework can seamlessly handle additional sparsity constraints such as total variation

and allows for parallel imaging and various k-space acquisition schemes. In this paper, we use radial golden angle trajectory since it is less sensitive to motion and is the standard choice for dynamic MRI.The optimization algorithm uses Alternating direction method of multipliers (ADMM) [6].

The remaining paper is arranged as follows: Section 2 provides a brief description of various approaches employed in dynamic MRI reconstruction. Section 2.1 provides some background of kernel methods. The proposed method is expained in Section 3 and the results are given in Section 4. Section 5 concludes the paper.

2 Background

The multi-coil dynamic MRI data $Y = [y_1, \cdots, y_n]$, is modeled as

$$Y = AX + \eta, \tag{1}$$

where $A = \mathcal{F}C$, $\mathcal{F}$ and C are the under-sampled Fourier transform and coil sensitivity maps, X is the Casorati matrix formed by concatenating the vectorized images, $X = [x_1, \ldots, x_n]$, and η is the noise. Reconstructing of the dynamic image matrix X, from the under-sampled MRI k-space data Y is ill-posed and can only be solved by applying regularization. CS-based methods use the sparsity of the MR images for reconstruction [25]:

$$X^* = \underset{X}{\operatorname{argmin}} \|AX - Y\|^2 + \beta \|SX\|_1, \tag{2}$$

where S is the sparsity inducing transform with regularization parameter β, which determines the tradeoff between data consistency and sparsity. This compressed sensing based formulation can reconstruct the signal even though the k-space data is acquired under-sampled by solving the l_1 minimization problem in Equation (2). Minimizing l_1 norm ensures sparsity. Sparsity can be applied in both the spatial and temporal domains. The well known sparsity transform is the finite-difference transform, which measures the sum of absolute variations in the image intensity. To enforce sparsity between images that are in the same motion state but are temporally far, researchers have looked at various approaches which either require self gating of repeated sampling of the k-space location [13, 35, 44].

Equation (2) is also called the analysis formulation of the sparse representation. Synthesis model is another sparse representation model, which attempts to reconstruct images using a linear combination of few basis functions ($X = W\alpha$): [11]:

$$\alpha^* = \underset{\alpha}{\operatorname{argmin}} \|AW\alpha - Y\|^2 + \beta \|\alpha\|_0, \tag{3}$$

Equation (3) is non-convex, which is made convex by replacing l_0 norm with the l_1 norm. k-t Blast [43] and k-t Sparse [24] employ the synthesis model to reconstruct images. K-t Blast uses training data to learn the temporal

basis functions, whereas k-t Sparse employs compressed sensing to improve the reconstruction. Similar to the synthesis model, low rank of the dynamic MR images can also be exploited to reconstruct the images:

$$X^* = \underset{X}{\operatorname{argmin}} \|AX - Y\|^2 + \beta\, rank(X), \tag{4}$$

The above formulation is used with Karhunen-Louve transform (KLT) [15, 20, 22, 26]. Next section will go over the basics of kernel method.

2.1 Kernel Method Basics

Kernel methods are a widely used class of algorithms for analyzing data. In kernel methods, data is implicitly mapped to a high dimension feature space which is more suitable for finding interesting correlations between data points [3, 30, 39]. Explicit computation of the feature space is avoided by employing the kernel trick: a kernel is a function $k : \mathbb{R}^d \times \mathbb{R}^d \to \mathbb{R}$, which implicitly defines a mapping $\phi : \mathbb{R}^d \to \mathcal{H}$, where $\mathcal{H}$ is a high dimensional feature space and the following equation holds:

$$k(x_i, x_j) = \langle \phi(x_i), \phi(x_j) \rangle. \tag{5}$$

Equation (5) allows the computation of the inner product between data points in the feature space through the kernel k. Let K be the kernel matrix, with values $K_{ij} = k(x_i, x_j)$. The feature space that satisfies the inner product property of Equation (5) can be obtained by the eigenvalue decomposition of kernel matrix $K = U\Lambda U^T$, where U and Λ are eigenvectors and eigenvalues of the kernel matrix. The feature space embedding satisfying (5) is given by

$$K = U\Lambda U^T = U\Lambda^{\frac{1}{2}}(U\Lambda_x^{\frac{1}{2}})^T = \Phi^T\Phi, \tag{6}$$

where $\Phi = \sqrt{\Lambda}U^T$ is the feature space matrix q, whose columns contain the feature space representation of the data points, $\Phi = [\phi(x_i), \cdots, \phi(x_n)]$. The mapping of a new text point x to feature space is obtained using the Nyström approximation method [5]

$$\phi(x) = \frac{1}{\sqrt{\Lambda}} U^T k_x, \tag{7}$$

where $k_x = [k(x, x_1), \cdots, k(x, x_n)]^T$.

2.1.1 Pre-image Problem

Pre-image problem relates to finding the mapping of a point $\psi \in \mathcal{H}$ in the feature space to the point x in the input space, such that $\phi(x) = \psi$. The exact pre-image might not exist, in genernal. Therefore, the pre-image methods seek an approximate pre-image satisfying the following optimality criteria:

$x^* = \underset{x}{\operatorname{argmin}} \|\phi(x) - \psi\|^2$. It is assumed that ψ is a linear combination of sample points $\psi = \sum_{i=1}^{n} \alpha_i \phi(x_i)$. The optimal x is then given by [40]

$$x = \frac{\sum_{i=1}^{n} \alpha_i k(x, x_i) x_i}{\sum_{i=1}^{n} \alpha_i k(x, x_i)}, \tag{8}$$

leading to the fixed point iteration scheme [40]. The iteration scheme is susceptible to local minima and sensitive to initialization. Arias et al. [2] propose a one step alternate to the fixed point iteration scheme. In the alternate methods, the kernel values are approximated by inverting the Nystrom extension (Equation (7)):

$$k_x = U\sqrt{\Lambda}\psi.$$

The pre-image x of a point ψ in the feature space is obtained by using the above approximation of the kernel values in Equation (8). In this paper, we are only interested in finding the low rank pre-image of the sample points x_i. In that case, the pre-image expression can be further simplified as follows:

$$R = \frac{XUU^T}{1_n 1_n^T UU^T}, \tag{9}$$

where 1_n is a vector of all ones, and the division in (9) is carried out element wise. In the remainder of the paper, Equation (9) is used for computing the pre-image.

3 Methodology

Given the under-sampled k-space data, the reconstruction is obtained by solving the following regularized optimizing problem.

$$X^* = \underset{X}{\operatorname{argmin}} \|AX - Y\|^2 + \beta \operatorname{rank}(\Phi), \tag{10}$$

where $\Phi = [\phi(x_1), \cdots, \phi(x_n)]$ is the feature space representation of the dynamic image series as obtained from Equation (6). A central assumption here is that the high dimensionality of the data is superficial and the data may be described as a function of few underlying parameters. The minimum rank decomposition of the feature space representation of the data matrix in Equation (10) is an effective strategy to learn the parameter space of the low-dimensional manifold. When the kernel used is linear, i.e $k(x_i, x_j) = x_i^T x_j$, the optimization problem (10) reduces to the one used in [22]. Various non-linear kernels can be used, such as the Gaussian kernel. To make the problem tractable, nuclear norm ($\|\cdot\|_*$) is used instead of rank minimization. The nuclear norm of the matrix Φ is the sum of the singular values of Φ. The singular values of Φ are equal to the square root of the singular values of the kernel matrix

$K = \Phi^T\Phi$, and therefore $\|\Phi\|_* = \sum_i \sqrt{\Lambda_{ii}}$. The relaxed optimization problem using nuclear norm is as follows:

$$X^* = \underset{X}{\operatorname{argmin}} \|AX - Y\|^2 + \beta\|\Phi\|_*. \tag{11}$$

The unconstrained optimization problem (11) is first converted to an equivalent constrained one using a technique called variable splitting. The idea behind variable splitting is to decouple the minimization of the two functions in Equation (11) by replacing Φ with an auxiliary variable $\Psi \in \mathcal{H}$ under the constraint that $\Psi = \phi(X)$.

$$\begin{aligned} X^* = \underset{X,R}{\operatorname{argmin}} &\|AX - Y\|^2 + \beta\|\Psi\|_* \\ \text{subject to} \quad &\phi(X) = \Psi \end{aligned} \tag{12}$$

The constraint in Equation (12) is defined in the feature space. To simplify the optimization, we define an equivalent constraint in the input space. Let R be the pre-image of Ψ (i.e $\Phi(R) = \Psi$) found using the technique described in Section 2.1, then Equation (12) becomes

$$\begin{aligned} X^* = \underset{X,R}{\operatorname{argmin}} &\|AX - Y\|^2 + \beta\|R\|_* \\ \text{subject to} \quad &X = R. \end{aligned} \tag{13}$$

The unconstrained form of the function using AL is

$$\begin{aligned} \mathcal{L}(X, R, \lambda) = \|AX - Y\|^2 + \beta\|R\|_* + \lambda^T(X - R) + \\ \frac{\rho}{2}\|X - R\|^2 \end{aligned} \tag{14}$$

where ρ is the penalty parameter penalizing the quadratic penalty term. The AL formulation guarantees convergence to the constraint optimization problem (13) without requiring high values for penalty parameter ρ [31]. Finally, Equation (14) is solved using ADMM [6, 10]. In ADMM, X and R are updated alternatively. Methods based on ADMM are widely used in the compressed sensing-based reconstruction frameworks [1, 22, 36, 47].

The first sub-problem ($X^{k+1} := \underset{X}{\operatorname{argmin}}\, \mathcal{L}(X, R^k, \lambda^k)$)

$$X^{k+1} := \underset{X}{\operatorname{argmin}}\, \|AX - Y\|^2 + \lambda^T(X - R) + \frac{\rho}{2}\|X - R\|^2, \tag{15}$$

is solved using a few iterations of conjugate gradient descent. Other sparsity constraints can be easily added in the optimization subproblem. It is often useful to include the finite-difference sparsifying transform (also known as total variation regularization) in the objective function [25].

The second sub-problem is

$$R^{k+1} = \underset{R^k}{\operatorname{argmin}}\, \beta\|R^k\|_* + \frac{\rho}{2}\|X^k + \frac{\lambda^k}{\rho} - R^k\|^2. \tag{16}$$

The equivalent formulation in the feature space is

$$\Psi^{k+1} = \underset{\Psi^k}{\operatorname{argmin}}\, \beta\|\Psi^k\|_* + \frac{\rho}{2}\|\Phi(X^k + \frac{\lambda^k}{\rho}) - \Psi^k\|^2. \tag{17}$$

Equation (17) looks cumbersome, however, the solution to (17) can be expressed in a closed form [45]

$$\Psi^{k+1} = D_\beta \sqrt{D} U^T, \tag{18}$$

where U and D are the eigenvectors and eigenvalues of the kernel matrix K formed from the data matrix $(X^k + \frac{\lambda^k}{\rho})$ and D_β is diagonal matrix with values

$$D_\beta(i,i) = \begin{cases} 1 - \frac{\beta}{\rho\sigma_i} & \text{if}\, \sigma_i > \frac{\beta}{\rho} \\ 0 & \text{otherwise} \end{cases}$$

where σ_i are the diagonal elements of D. Compare the feature space embedding Φ (6) to its low rank embedding Ψ (18). The low rank embedding is obtained by multiplying the feauture space embedding by D_β. The pre-image of Ψ can then be easily computed using Equation (9). Finally, λ is updated by

$$\lambda^{k+1} := \lambda^k + \rho(X^{k+1} - R^{k+1}) \tag{19}$$

The whole algorithm is listed in Algorithm 1.

3.1 Implementation

The proposed ADMM-based algorithm was implemented in Matlab on a Ubuntu workstation with intel core i7-6700K processor. Subproblem (15) was solved using non-linear conjugate gradient descent with backtracking line search [25]. As mentioned before, few iterations of the CGD were carried out, as ADMM converges even when sub-problems are approximately solved [6]. The second sub-problem (16) can be solved analytically. It requires singular value decomposition of the kernel matrix of size $n \times n$, where n is the number of dynamic frames to reconstruct. k-t SLR [22], which finds linear correlation between the dynamic frames in the input space also requires singular value decomposition of $n \times n$ matrix. In this regard, no additional computational effort is required to obtain non-linear correlations in the feature space. The proposed algorithm is summarized below. ADMM converges to an acceptable accuracy within few iterations [6]. In all the experiments in Section 4, we ran at most ten ADMM iterations to obtain reasonable results.

Data: dynamic MRI data
Result: Reconstructed Casorati matrix X
Initialize X by the inverse Fourier transform of the gridded k-space measurements;
while *stopping criteria not met* **do**
  Solve problem (15) by running few iterations of non-linear conjugate gradient descent;
  Compute low-rank approximation (18);
  Computer pre-image (9);
  Updata λ (19)
end

Algorithm 1: Proposed ADMM-based Optimization Algorithm

4 Results

In this section we compare the reconstruction performance of the proposed method. The reconstruction error was gauged using the signal to error ratio (SER), which is defined as:

$$SER = -10\, log_{10} \frac{\|X_{rec} - X_{orig}\|_F^2}{\|X_{orig}\|_F^2}, \tag{20}$$

where $\|\cdot\|_F$ is the Frobenius norm, X_{rec} and X_{orig} are the reconstructed and the original Casorati matrix. The k-space samples are acquired using golden angle radial trajectory, where radial profile lines are spaced at a constant increment of 111.25^0. This scheme insures that the k-space is uniformly sampled for any consecutive number of profile lines [48]. We evaluated the proposed method on both the synthetic and *in vivo* datasets against the following methods:

k-t SLR [22] k-t SLR poses the recovery of the dynamic image series X as a low rank matrix recovery problem similar to Equation (18). k-t SLR exploits linear correlations between the image frames. By enforcing low rank constraint in the non-linear feature space, our method can learn non-linear correlations between the data frames and hence better reconstruction of the images. Matlab code provided by the author was used.

Spatio-Temporal total variation (TV) regularization Total variation regularization exploits the sparsity of the gradients and is often included in the objective function even when other sparsifying transforms are present [25]. In dynamic MRI, TV regularization can be applied in both the spatial and temporal domains. The TV regularized objective function is

$$\underset{X}{\operatorname{argmin}} \|AX - Y\|^2 + \beta \left\| \sqrt{|D_x X|^2 + |D_y X|^2 + |X D_t|^2} \right\|_1$$

where D_x, D_y, D_t are finite difference operators in the spatial (x, y) and temporal domains. It is also part of the objective function in the k-t SLR framework and is also included in the proposed framework. Comparing with TV regularization alone will help in gauging the improvement or otherwise brought in by the additional low rank constraint. The TV regularization is implemented using [22, 47].

Gridding All methods are initialized with zero-filled reconstruction of the radial profile lines.

4.1 Pre-image Computation Comparison

Before proceeding to the results, we provide few experiments in this section to demonstrate that the use of feature space representation is better able to capture the correlations in the dynamic MRI data. The vectorized images of PINCAT numerical phantom [41] are stacked together to obtain the Casorati matrix X of size $128^2 \times 50$. The data matrix X can be decomposed using the singular value decomposition $X = U\Sigma V^H$. Such a decomposition is used in multiple KLT based reconstruction algorithms [15, 20, 22, 26, 33]. The rows of ΣV^H and U can be considered as the temporal basis functions and the spatial weights respectively. In principal component analysis parlance, the columns of U are the basis of the transformed space and the columns of ΣV^H are the projections onto the basis functions. Since the dynamic data matrix X is highly correlated, the pre-image can be computed using the few most significant singular values. Moreover, by exploiting the correlation in the non-linear feature space Φ, we expect to require even fewer basis functions. To demonstrate that, we compute the pre-image using the 15 most significant singular values. Moreover, the original image is also corrupted by setting few pixel intensity values to zero. Figures 1(a) and 1(b) show the original and the corrupted image. The pre-image computed using the KLT and the feature space representation (9) is shown in Figures 1(a) and 1(d). The figure clearly shows that the feature space pre-image is better than the linear KLT based pre-image.

Figure 2 shows the temporal intensity profiles corresponding to the white line drawn on the left most image. The temporal intensity profiles are sorted according to the most significant temporal basis function for both the feature space and KLT representation (middle and right most image respectively). As a result of sorting, similar temporal profiles are clustered together. The figure shows that the clustering of the temporal profiles achieved by the feature space representation is better than the KLT method. The white arrows highlight few locations where the clustering of the similar intensity profiles produces smooth overall image as compared to the KLT representation.

4.2 Synthetic Data

We evaluated the proposed method on a physiologically improved non-uniform cardiac torso (PINCAT) numerical phantom [41], made available from [22]. The data simulates a free breathing first-pass myocardial perfusion dynamics. The time series data contains 50 frames of spatial size 128×128.

The proposed method is evaluated at various accelerations and noise levels. The PINCAT phantom has spatial size of 128×128. A fully sampled k-space

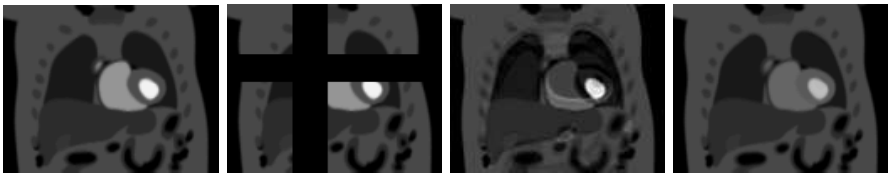

(a) (b) (c) (d)

Fig. 1 Pre-image computation using 15 most significant singular values. (a): a frame from the PINCAT numerical phantom [41] corrupted by setting few pixel intensity values to zero in (b), (c) Pre-image of the frame using KLT and (d) Pre-image using the feature space representation (9). The feature space compact representation has been better able to recover the corrupted signal.

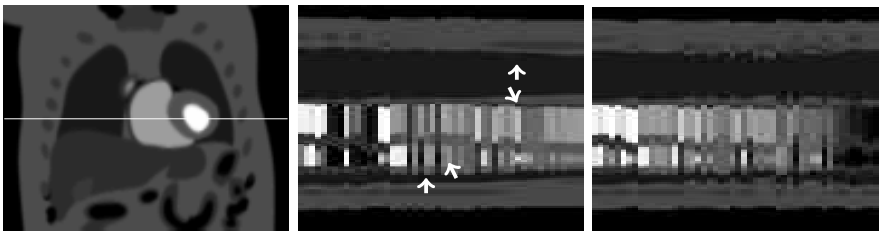

Fig. 2 Temporal intensity profiles sorted according to the most significant temporal basis function. [Left]: A frame from PINCAT data set. The temporal intensity profiles drawn in the following images correspond to the white line drawn on the image. [Middle]: temporal intensity profiles sorted according to the feature space representation. The white arrows highlight few locations where the clustering of the similar intensity profiles produces a smooth overall image as compared to the KLT representation. [Right]: KLT representation

data will consists of 128 lines and therefore using for example 24 lines in the reconstruction will result in the acceleration level of 5.33.

Figure 3 shows the SER versus acceleration plot for various reconstruction methods. At higher acceleration levels, k-t SLR is not able to effectively utilize the correlations between the dynamic image series and no significant improvement over TV norm is achieved. The proposed method, by imposing a low rank structure in the non-linear feature space, out performs other methods at all acceleration levels. All methods are initialed by the reconstruction obtained by zero-filled reconstruction (gridding). The SER of gridding reconstruction is also shown in the figure for reference.

In the second experiment, zero mean Gaussian random noise is added to the k-space measurement. The standard deviation of the noise is adjusted so that the signal to noise ratio (SNR $= 10\,log\,\frac{\sigma^2_{\text{signal}}}{\sigma^2_{\text{noise}}}$) varies from 28 to 50 decibels. The k-space is sampled at 24 profile lines per frame (acceleration of 5.3) for all noise levels. Figure 4 shows the performance of the proposed and comparison methods. The proposed algorithm produces reconstructions with higher SER than the comparison methods at all noise levels. The difference in performance between the proposed and the comparison methods is more pronounced at lower SNR. Figure 5 shows a reconstructed frame of the dynamic image series

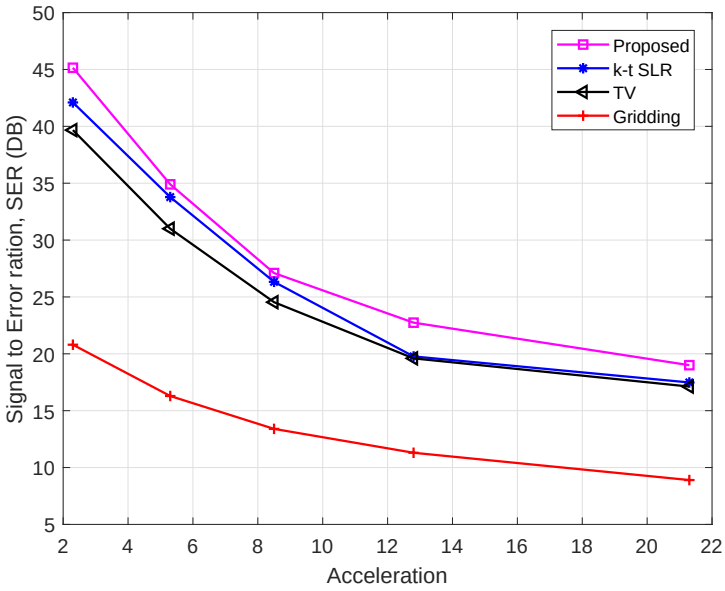

Fig. 3 Signal-to-error ratio versus acceleration plot for various reconstruction methods on PINCAT phantom. The proposed method consistently out performs other comparison methods.

along with its error map. The error map shows that the the proposed method produces reconstructions having fewer artifacts than the comparison methods.

4.3 First-Pass Myocardial Perfusion *in vivo* Data

The *in vivo* data was obtained from [22]. The data represents the first-pass myocardial perfusion real time MRI sequence ($n_x = 190, n_y = 90, t = 70$). The proposed and the comparison methods are evaluated at the acceleration level of 19. All methods are initialized by the zero-filled reconstruction obtained by interpolating the golden angle radial profile lines to the Cartesian grid and using the inverse Fourier transform to reconstruct the images. Figure 6(a) shows few fully sampled frames at different contrast enhancement phases. The white vertical lines in Figure 6(f) represent the location in time of the frames. Figures 6(b)-6(e) show the reconstructed images using the comparison and the proposed methods. The regularization parameters for all methods were fine tuned to obtain maximum SER for fair comparison. The proposed method obtains the best SER of 18.27. Some of the obvious artifacts are also highlighted in the figure by using the arrows. The k-t SLR method could not effectively utilize the low rank structure of the dynamic image data due to the fast acceleration levels. The temporal intensity profiles corresponding to the white horizontal line in Figure 6(a) are shown in Figures 6(f)-6(j) of the

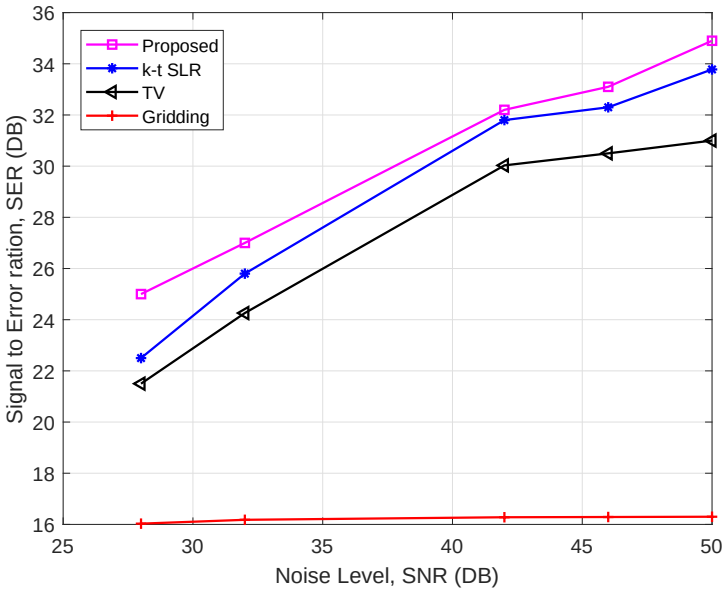

Fig. 4 Signal-to-error ratio versus noise level for various reconstruction methods on PINCAT phantom. The signal-to-noise ratio of k-space measurements is varied from 28 to 50 decibels. The k-space is sampled at 24 profile lines per frame (acceleration of 5.3) for all noise levels. The proposed algorithm produces reconstructions with higher SER. The difference in performance is more pronounced at lower SNR

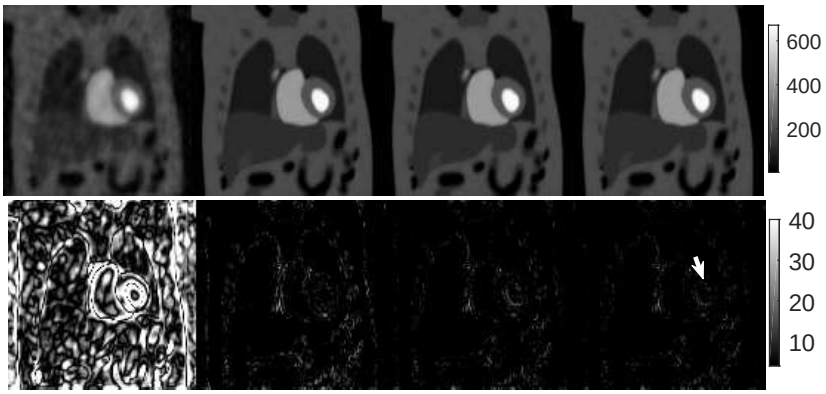

Fig. 5 A reconstructed frame of PINCAT Phantom and its error map. [Images from left to right]: Gridding reconstruction, TV penalty, k-t SLR [22] and the proposed method. The proposed method produces reconstructions with fewer artifacts.

comparison and the proposed methods. The temporal profiles of the proposed method closely follows the fully sampled profile lines.

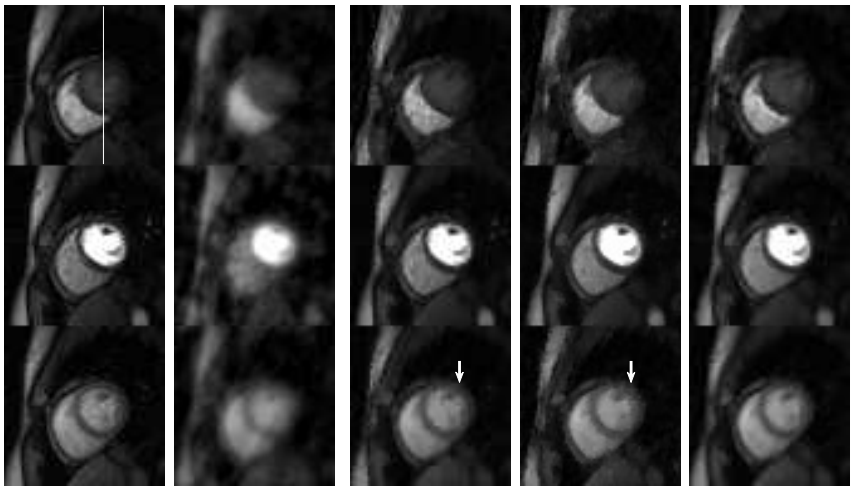

(a) Fully sampled (b) Gridding, SER = 10.81 (c) TV penalty, SER = 17.05 (d) k-t SLR [22], SER = 16.52 (e) Proposed Method, SER = 18.27

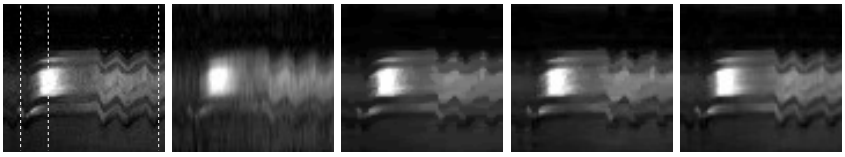

(f) (g) (h) (i) (j)

Fig. 6 Reconstruction of first-pass myocardial perfusion sequence. (a) A few fully sampled frames at contrast enhancement phases indicated by white vertical lines in (f). (b-e) Reconstructed images using various methods. The proposed method obtains the best SER of 18.27. Some of the artifacts are also highlighted by using the arrows. (g-l) Temporal intensity profiles corresponding to the white line in (a) of the various methods. The temporal intensity profile of the proposed method closely follows the fully sampled profile lines.

4.4 Liver DCE-MRI

The liver DCE-MRI data, obtained from [13], contains contrast-enhancement phases and respiratory motion. The data was acquired by 12-element body matrix coil using the 3D stack-of-stars radial trajectory with golden angle rotation. The reconstruction of only one slice is shown in this section. The data contains 1100 radial profiles, which were continuously acquired and grouped in to multiple respiratory motion and contrast enhancement states by using the projection-based respiratory motion detection approach described in [13]. In total, there were 11 contrast-enhancement phases, each containing 4 respiratory motion states with 25 radial profiles. XD-Grasp [13] then reconstructs the dynamic images by applying the total variation regularization in both the respiratory and the contrast-enhancement dimensions. Figure 7(a) shows the result of one contrast-enhancement phase containing 4 respiratory motion

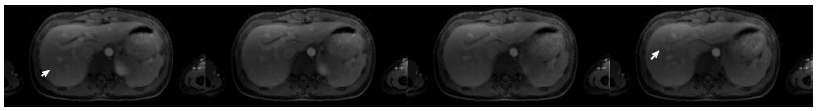

(a) XD-Grasp Reconstruction[13]

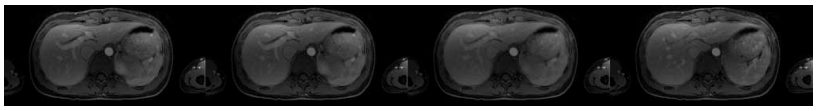

(b) Proposed Algorithm Reconstruction

Fig. 7 Liver DCE-MRI. Reconstruction of one contrast-enhancement phase containing four respiratory motion states. XD-Grasp [13] applies total variation regularization in both the respiratory and contrast-enhancement dimensions. The proposed algorithm applies low rank constraint in the feature space to reconstruct the images. The reconstruction quality of the proposed method enhanced as highlighted by the arrows. XD-Grasp looses some details due to over smoothing.

states. The proposed algorithm reconstructs the images by using 25 radial profiles per image and the low rank constraint in the feature space. The results are shown in Figure 7(b). As the figure shows, the reconstruction quality of the proposed method is enhanced. In some areas, highlighted by the arrows, XD-Grasp actually looses some details due to over smoothing.

5 Conclusion

Kernel methods in statistical learning theory provide powerful techniques for analyzing high-dimensional data. The basic idea behind kernel methods is to map the data non-linearly to a higher dimensional feature space where linear algorithms are applied. In this paper, we exploit the non-linear correlation between dynamic MR images using kernel methods. Specifically, the dynamic sequence is mapped to the feature space where low rank constraint is enforced. The algorithm simultaneously learns the temporal basis and the spatial weights of the non-linear feature space and does not require any training data. The algorithm exploits the non-linear correlations without the computational burden as the computational complexity is similar to the linear low rank-based algorithms. The optimization is carried out using variable splitting and ADMM and achieves convergence within few iterations. Evaluations are performed on synthetic as well as *in vivo* datasets.

References

1. Afonso MV, Bioucas-Dias JM, Figueiredo MA (2010) Fast image recovery using variable splitting and constrained optimization. IEEE Transactions on Image Processing 19(9):2345–2356

2. Arias P, Randall G, Sapiro G (2007) Connecting the out-of-sample and pre-image problems in kernel methods. In: Computer Vision and Pattern Recognition, 2007. CVPR'07. IEEE Conference on, IEEE, pp 1–8
3. Arif O, Vela P, Daley W (2010) Pre-image problem in manifold learning and dimensional reduction methods. In: 2010 Ninth International Conference on Machine Learning and Applications, IEEE, pp 921–924
4. Belkin M, Niyogi P (2003) Laplacian eigenmaps for dimensionality reduction and data representation. Neural computation 15(6):1373–1396
5. Bengio Y, Paiement J, Vincent P, Delalleau O, Roux NL, Ouimet M (2004) Out-of-sample extensions for LLE, isomap, MDS, eigenmaps, and spectral clustering. In: Advances in Neural Information Processing Systems, p 177
6. Boyd S, Parikh N, Chu E, Peleato B, Eckstein J (2011) Distributed optimization and statistical learning via the alternating direction method of multipliers. Foundations and Trends® in Machine Learning 3(1):1–122
7. Buerger C, Clough RE, King AP, Schaeffter T, Prieto C (2012) Nonrigid motion modeling of the liver from 3-d undersampled self-gated golden-radial phase encoded mri. IEEE transactions on medical imaging 31(3):805–815
8. Chen X, Usman M, Baumgartner CF, Balfour DR, Marsden PK, Reader AJ, Prieto C, King AP (2017) High-resolution self-gated dynamic abdominal mri using manifold alignment. IEEE transactions on medical imaging 36(4):960–971
9. Donoho DL (2006) Compressed sensing. IEEE Transactions on information theory 52(4):1289–1306
10. Eckstein J, Bertsekas DP (1992) On the douglasrachford splitting method and the proximal point algorithm for maximal monotone operators. Mathematical Programming 55(1):293–318
11. Elad M, Milanfar P, Rubinstein R (2007) Analysis versus synthesis in signal priors. Inverse problems 23(3):947
12. Feng L, Grimm R, Block KT, Chandarana H, Kim S, Xu J, Axel L, Sodickson DK, Otazo R (2014) Golden-angle radial sparse parallel mri: Combination of compressed sensing, parallel imaging, and golden-angle radial sampling for fast and flexible dynamic volumetric mri. Magnetic resonance in medicine 72(3):707–717
13. Feng L, Axel L, Chandarana H, Block KT, Sodickson DK, Otazo R (2016) Xd-grasp: Golden-angle radial mri with reconstruction of extra motion-state dimensions using compressed sensing. Magnetic resonance in medicine 75(2):775–788
14. Glover GH, Pauly JM (1992) Projection reconstruction techniques for reduction of motion effects in mri. Magnetic resonance in medicine 28(2):275–289
15. Haldar JP, Liang ZP (2010) Spatiotemporal imaging with partially separable functions: A matrix recovery approach. In: Biomedical Imaging: From Nano to Macro, 2010 IEEE International Symposium on, IEEE, pp 716–719

16. King AP, Buerger C, Tsoumpas C, Marsden PK, Schaeffter T (2012) Thoracic respiratory motion estimation from mri using a statistical model and a 2-d image navigator. Medical image analysis 16(1):252–264
17. Larkman DJ, Nunes RG (2007) Parallel magnetic resonance imaging. Physics in medicine and biology 52(7):R15
18. Larson AC, White RD, Laub G, McVeigh ER, Li D, Simonetti OP (2004) Self-gated cardiac cine mri. Magnetic Resonance in Medicine 51(1):93–102
19. Li X, Arlinghaus LR, Ayers GD, Chakravarthy AB, Abramson RG, Abramson VG, Atuegwu N, Farley J, Mayer IA, Kelley MC, et al. (2014) Dce-mri analysis methods for predicting the response of breast cancer to neoadjuvant chemotherapy: Pilot study findings. Magnetic resonance in medicine 71(4):1592–1602
20. Liang ZP (2007) Spatiotemporal imagingwith partially separable functions. In: Biomedical Imaging: From Nano to Macro, 2007. ISBI 2007. 4th IEEE International Symposium on, IEEE, pp 988–991
21. Lin W, Guo J, Rosen MA, Song HK (2008) Respiratory motion-compensated radial dynamic contrast-enhanced (dce)-mri of chest and abdominal lesions. Magnetic resonance in medicine 60(5):1135–1146
22. Lingala SG, Hu Y, DiBella E, Jacob M (2011) Accelerated dynamic mri exploiting sparsity and low-rank structure: kt slr. IEEE transactions on medical imaging 30(5):1042–1054
23. Liu J, Spincemaille P, Codella NC, Nguyen TD, Prince MR, Wang Y (2010) Respiratory and cardiac self-gated free-breathing cardiac cine imaging with multiecho 3d hybrid radial ssfp acquisition. Magnetic resonance in medicine 63(5):1230–1237
24. Lustig M, Santos JM, Donoho DL, Pauly JM (2006) kt sparse: High frame rate dynamic mri exploiting spatio-temporal sparsity. In: Proceedings of the 13th Annual Meeting of ISMRM, Seattle, vol 2420
25. Lustig M, Donoho D, Pauly JM (2007) Sparse mri: The application of compressed sensing for rapid mr imaging. Magnetic resonance in medicine 58(6):1182–1195
26. Majumdar A, Ward RK (2011) An algorithm for sparse mri reconstruction by schatten p-norm minimization. Magnetic resonance imaging 29(3):408–417
27. Nakarmi U, Wang Y, Lyu J, Ying L (2015) Dynamic magnetic resonance imaging using compressed sensing with self-learned nonlinear dictionary (nl-d). In: 2015 IEEE 12th International Symposium on Biomedical Imaging (ISBI), IEEE, pp 331–334
28. Nakarmi U, Zhou Y, Lyu J, Slavakis K, Ying L (2016) Accelerating dynamic magnetic resonance imaging by nonlinear sparse coding. In: 2016 IEEE 13th International Symposium on Biomedical Imaging (ISBI), IEEE, pp 510–513
29. Nakarmi U, Wang Y, Lyu J, Liang D, Ying L (2017) A kernel-based low-rank (klr) model for low-dimensional manifold recovery in highly accelerated dynamic mri. IEEE transactions on medical imaging 36(11):2297–2307

30. Nawaz MZ, Arif O (2016) Robust kernel embedding of conditional and posterior distributions with applications. In: 2016 15th IEEE International Conference on Machine Learning and Applications (ICMLA), IEEE, pp 39–44
31. Nocedal J, Wright SJ (2006) Sequential quadratic programming. Springer
32. Otazo R, Kim D, Axel L, Sodickson DK (2010) Combination of compressed sensing and parallel imaging for highly accelerated first-pass cardiac perfusion mri. Magnetic Resonance in Medicine 64(3):767–776
33. Pedersen H, Kozerke S, Ringgaard S, Nehrke K, Kim WY (2009) k-t pca: Temporally constrained k-t blast reconstruction using principal component analysis. Magnetic resonance in medicine 62(3):706–716
34. Peters DC, Lederman RJ, Dick AJ, Raman VK, Guttman MA, Derbyshire JA, McVeigh ER (2003) Undersampled projection reconstruction for active catheter imaging with adaptable temporal resolution and catheter-only views. Magnetic resonance in medicine 49(2):216–222
35. Poddar S, Jacob M (2016) Dynamic mri using smoothness regularization on manifolds (storm). IEEE transactions on medical imaging 35(4):1106–1115
36. Ramani S, Fessler JA (2011) Parallel mr image reconstruction using augmented lagrangian methods. IEEE Transactions on Medical Imaging 30(3):694–706
37. Roweis ST, Saul LK (2000) Nonlinear dimensionality reduction by locally linear embedding. science 290(5500):2323–2326
38. Santelli C, Nezafat R, Goddu B, Manning WJ, Smink J, Kozerke S, Peters DC (2011) Respiratory bellows revisited for motion compensation: preliminary experience for cardiovascular mr. Magnetic resonance in medicine 65(4):1097–1102
39. Schölkopf B, Smola A, Müller KR (1998) Nonlinear component analysis as a kernel eigenvalue problem. Neural computation 10(5):1299–1319
40. Scholköpf B, Smola A, Muller KR (1998) Nonlinear component analysis as a kernel eigenvalue problem. Neural Computation pp 1299–1319
41. Sharif B, Bresler Y (2007) Physiologically improved ncat phantom (pincat) enables in-silico study of the effects of beat-to-beat variability on cardiac mr. In: Proceedings of the Annual Meeting of ISMRM, Berlin, vol 3418
42. Trémoulhéac B, Dikaios N, Atkinson D, Arridge SR (2014) Dynamic mr image reconstruction–separation from undersampled k-space via low-rank plus sparse prior. IEEE transactions on medical imaging 33(8):1689–1701
43. Tsao J, Boesiger P, Pruessmann KP (2003) k-t blast and k-t sense: Dynamic mri with high frame rate exploiting spatiotemporal correlations. Magnetic resonance in medicine 50(5):1031–1042
44. Usman M, Vaillant G, Atkinson D, Schaeffter T, Prieto C (2014) Compressive manifold learning: Estimating one-dimensional respiratory motion directly from undersampled k-space data. Magnetic resonance in medicine 72(4):1130–1140
45. Wang VJ, Castanon D (2011) Kernel low rank representation. Boston University-Center for Information & Systems Engineering, Tech Rep

46. Wang Y, Ying L (2014) Undersampled dynamic magnetic resonance imaging using kernel principal component analysis. In: 2014 36th Annual International Conference of the IEEE Engineering in Medicine and Biology Society, IEEE, pp 1533–1536
47. Wang Y, Yang J, Yin W, Zhang Y (2008) A new alternating minimization algorithm for total variation image reconstruction. SIAM Journal on Imaging Sciences 1(3):248–272
48. Winkelmann S, Schaeffter T, Koehler T, Eggers H, Doessel O (2007) An optimal radial profile order based on the golden ratio for time-resolved mri. IEEE transactions on medical imaging 26(1):68–76